Traveling-Wave Photodetectors for High-Power, Large-Bandwidth Applications

Vincent M. Hietala, *Member, IEEE,* G. Allen Vawter, *Member, IEEE,* T. M. Brennan, and B. E. Hammons

Abstract—**The traveling-wave photodetectors (TWPD) discussed here offer theoretical quantum efficiencies approaching 100% while maintaining a very large electrical bandwidth. Additionally, they are capable of dissipating the high-power levels required for large dynamic range applications. In this paper, the power dissipation limit of the TWPD is explored. A small-signal steady-state model is developed that includes the effects of electrical propagation losses along the detector. Fabrication details are presented and experimental data shows a 3×1250 μm^2 detector with a 4.8-GHz bandwidth.**

I. Introduction

HIGH-POWER photodetectors are important in applications such as RF power generation using optical heterodyning and large dynamic range communication systems. This paper describes the modeling and fabrication of a traveling-wave photodetector (TWPD) that is capable of dissipating very large power levels while maintaining a high electrical bandwidth. The TWPD is a waveguide photodetector featuring an electrode geometry that is velocity matched to the optical signal. Such a detector was proposed by Taylor *et al.* [1] and recently pursued independently by several groups [2]–[5]. The TWPD presented in this paper is targeted at large power dissipation. This unique capability is achieved by the TWPD's large size. Large size, high bandwidth, and high quantum efficiency are inherent to this traveling-wave design.

The TWPD differs significantly from "traditional" photodetectors that are electrically lumped. The electrical bandwidth of a traditional photodetector is RC limited. Therefore, one strives to minimize capacitance, C, by reducing the detector's size. This has the unfortunate side effect of reducing the lumped detector's responsivity and maximum power dissipation. The TWPD avoids these limitations by being electrically distributed.

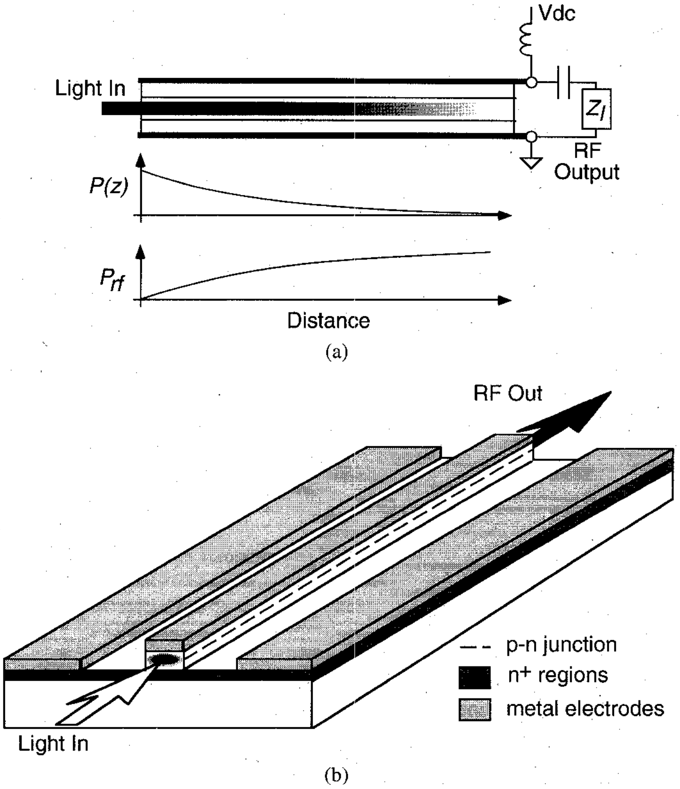

Fig. 1. Diagram of a TWPD. (a) Qualitative optical and RF power levels are shown along the detector'slength. (b) Physical diagram.

Fig. 1 illustrates the fundamental operation of the TWPD. Light is launched into an optical waveguide formed in the junction of a p-i-n diode (GaAs/AlGaAs in present design). The thickness of the absorbing region in the p-i-n diode is adjusted to set the absorption length in the optical waveguide. Use of a thin absorbing layer ($\approx$100 Å for GaAs @ 1.06 μm) permits for a very large absorption length due to its very low confinement factor of the guided light. The absorption is selected to be high enough for the majority of the light (say 95%) to be absorbed for high quantum efficiency, while still being low enough to allow for a large device length to achieve high power dissipation. Light is "detected" in an extended region along the p-i-n diode. This causes distributed current generation along the detector's length. The detector's metal electrodes are designed to allow for this generated current (RF signal) to "travel" in phase synchronism with the light. If velocity matching is achieved, the photo-generated distributed current will add at the detector's output.

II. Limits on Detected Power

The large power handling capability of the TWPD can best be understood by a simple analysis of the temperatures generated within the detector under static operation. The optical power distribution along a TWPD can be expressed as

$$|P(z)| = P_o e^{-2\alpha_o z} \tag{1}$$

where α_o is the field absorption coefficient of the optical mode propagating along the detector and P_o is the optical power

---

Manuscript received January 10, 1995; revised April 2, 1995. This work, performed at Sandia National Laboratories, was supported by the U.S. Department of Energy under contract DE-AC04-94AL85000.

The authors are with Sandia National Laboratories, Albuquerque, NM 87185-0603 USA.

IEEE Log Number 9413690.

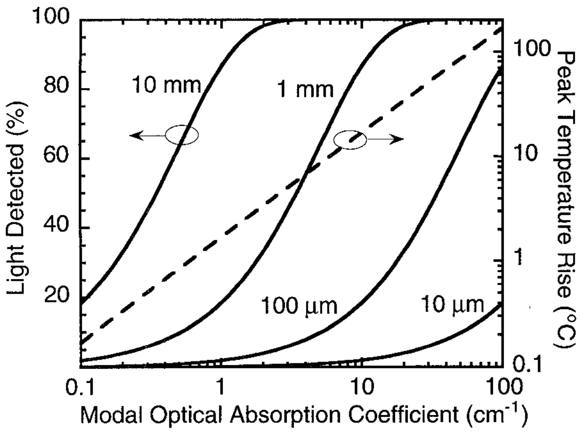

Fig. 2. Plot of percentage light detected as a function of the modal optical absorption coefficient for various detector lengths. Dashed line shows the peak temperature rise assuming $P_{\text{opt}} = 0.225$ W, 3×3 μm^2 guide dimension and a 50-μm-thick GaAs substrate.

entering the detector's input facet at $z = 0$. The optical power absorbed per unit length at any point along the detector is then

$$P_{\text{abs}}(z) = -\frac{d|P(z)|}{dz} = 2\alpha_o P_o e^{-2\alpha_o z}. \tag{2}$$

Assuming no back-reflection at the detector's far end, the total light detected is

$$P_{\text{abs},T} = \int_0^l P_{\text{abs}}(z)dz = P_o[1 - e^{-2\alpha_o l}] \tag{3}$$

where l is the detector's length. Fig. 2 shows the percentage detected light for several different detector lengths as a function of optical absorption coefficient. The light that is not detected is radiated at the far end of the detector.

To determine the temperature rise resulting from this absorbed light, the thermal impedance, θ, must be determined for a particular detector configuration. For the geometry of the TWPD shown in Fig. 1, the thermal impedance is approximately that of a planar line heat source on top of a dielectric slab [6]

$$\theta = \ln\left(\frac{8C}{\pi d}\right) \Big/ \pi k \tag{4}$$

where C is the substrate thickness, d is 1/2 the guide's width, and $k \approx 0.038$ W/°C · mm for GaAs at 60°C. For our detectors, $d = 1.5$ μm and $C = 50$ μm, which gives $\theta = 37.2$°C · mm/W. Due to the weak dependence of (4) on physical dimensions, this thermal impedance should be typical for most TWPD's.

The peak temperature rise occurs at the optical input of the detector where the absorbed optical power density is the largest [$P_{\text{abs}}(0)$ from (2)]. Notice that this peak power is controlled by the optical absorption coefficient, α_o, which can be controlled over a very large range. Therefore, in principle, a TWPD can be designed for any power level up to the catastrophic optical damage limit that typically occurs for a semiconductor facet at an incident optical power density of 5 MW/cm^2 [7] or if coupled into a 3×3 μm^2 waveguide, $P_o \approx 0.23$ W. Using this power level and the thermal impedance found above, the peak temperature rise caused by the absorbed light is shown as the dashed line in Fig. 2. This plot shows that significantly high temperatures will occur within the TWPD independent of the electrical bias applied. For example, assuming that 50°C is the maximum temperature rise that can be tolerated, the absorption coefficient must be less than 30 cm^{-1}. To have 95% of the light detected, the detector length must exceed 500 μm. Thus, for high power applications, the TWPD will necessarily be long.

With the optical power level used above and assuming the detector's quantum efficiency approaches 100%, the resulting photocurrent is over 190 mA at 1.06 μm optical wavelength. At a typical detector bias voltage of several tens of volts, this will result in an additional several watts of electrical power dissipation within the detector and a several fold increase in the detector's internal temperature.

Interestingly, with the optical power levels considered here, the resulting current levels could produce several Watts of RF into 50 Ω. The detector could be driven by the beat product from two lasers slightly detuned to produce the desired RF operating frequency (optical heterodyne). Such an approach has recently been demonstrated at frequencies up to 1.2 THz [8]. When operated at large optical powers, simple circuit analysis shows that this technique has a maximum wall-plug conversion efficiency (dc bias supply to RF) approaching 50% assuming the minimum possible dc bias voltage is used [9]. Unfortunately, this is not without a cost as seen in the above thermal calculations. If several Watts of RF power are desired, traditional high-bandwidth (small-size) photodetectors are inadequate and a detector like the TWPD is required.

III. SMALL-SIGNAL TWPD MODEL

A detailed frequency-domain model for the TWPD has been developed that incorporates electrical loss. This model was developed during the early part of this project [10], assumes small-signal steady-state operation, and has similar results to a time-domain model described recently by Giboney *et al.* [11].

Assuming no back reflection at the far end of the device (100% optical absorption), and excitation by two equal-power (P_o) lasers offset by the RF operating frequency, the optical intensity P_l within the photodetector can be described by

$$P_l(z,t) = 2P_o(1 + \sin(\omega_{\text{rf}} t - \beta_o z))e^{-2\alpha_o z} \tag{5}$$

where ω_{rf} is the angular RF beat frequency, z is the position along the length of the detector, and β_o is the propagation constant of the rf modulated light ($\beta_o \approx 2\pi n_o/\lambda_{\text{rf}}$). Dropping the DC term, (5) can be rewritten in phasor-wave notation at the RF-operating frequency ω_{rf}

$$p_l(z) = 2P_o e^{-\gamma_o z} \tag{6}$$

where

$$\gamma_o = 2\alpha_o + j\beta_o. \tag{7}$$

The exponential decay of the light as it propagates is due to photon absorption generating electrons and holes. The local current generated at any point along the detector is related

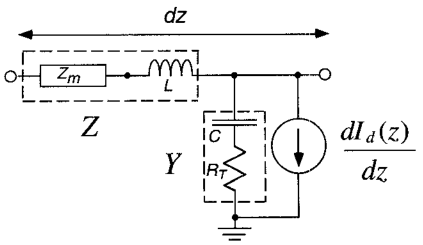

Fig. 3. Equivalent transmission-line circuit for TWPD.

to the amount of light absorbed at the point multiplied by a conversion factor

$$\frac{dI_d(z)}{dz} = -\frac{\xi e \lambda_o}{hc}\frac{d|p_l(z)|}{dz}e^{-j\beta_o z} \tag{8}$$

where ξ is the intrinsic quantum efficiency, e is the charge of an electron, h is Planck's constant, λ_o is the optical wavelength, and c is the speed of light. The intrinsic quantum efficiency is the fraction of electrons collected at the ohmic contacts to absorbed photons. Carrier transit times within the detector are neglected, allowing for (8) to be valid at all operating frequencies. Combining (6) and (8) gives

$$\frac{dI_d(z)}{dz} = k_o e^{-\gamma_o z} \tag{9}$$

where

$$k_o = \frac{4\alpha_o \xi e P_o \lambda_o}{hc}. \tag{10}$$

This distributed current is coupled to the electrical propagation along the detector as described by the time-harmonic telegraphist's equations

$$\frac{dV}{dz} = -ZI \tag{11}$$

and

$$\frac{dI}{dz} = -YV - \frac{dI_d(z)}{dz} \tag{12}$$

where the second term of (12) is the differential current source given by (9). The transmission line equivalent circuit is shown in Fig. 3. This model is only approximate since the current source is not in parallel with the capacitance. The incorporation of the current source as shown in Fig. 3 is appropriate provided that the transverse electrical loss is small compared to the electrical energy storage along the detector. This assumption is true for the electrode structure considered in the next section. Equations (11) and (12) can be combined to form a second order differential equation of the voltage (V) along the line

$$\frac{d^2V}{d^2z} - \gamma_e^2 V = Zk_o e^{-\gamma_o z} \tag{13}$$

where $\gamma_e = \sqrt{ZY}$ is the traditional electrical propagation constant along the detector.

A simple analytical solution of (13) results from variation of parameters

$$V(z) = V_1 e^{\gamma_e z} + V_2 e^{-\gamma_e z} + \frac{Zk_o}{\left(\gamma_o^2 - \gamma_e^2\right)}e^{-\gamma_o z}. \tag{14}$$

The first and second terms in the right hand side of (14) are the backward and forward propagating waves along a transmission line. The third term is the detected light's signal impressed along the line. Applying boundary conditions determines values for V_1 and V_2.

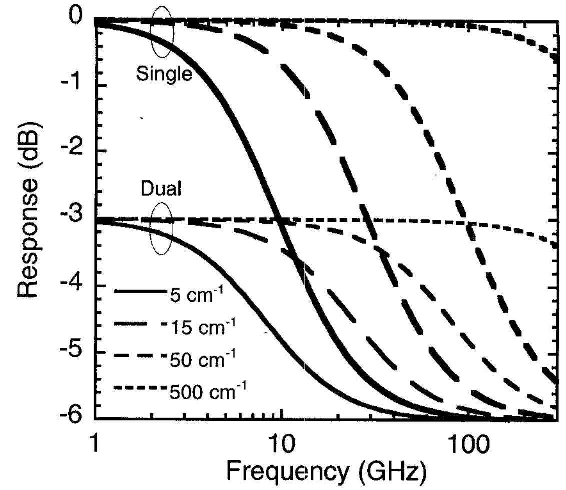

Fig. 4. Theoretical TWPD electrical response with output terminated in Z_o (thick lines) and with both input and output terminated in Z_o (thin lines) for several different optical absorption values.

Two sets of boundary conditions can be applied to (14) that are particularly informative. The first allows the input end of the detector (where the light enters the device) to be open with the output end terminated, as was shown in Fig. 1. The second set corresponds to the termination of both the input and the output ends in Z_o. The first set of boundary conditions corresponding to an open input and terminated output are

$$I(0) = 0 \quad \text{and} \quad \frac{V(l)}{I(l)} = Z_l. \tag{15}$$

Applying these boundary conditions to (14) gives

$$V_1 = \frac{k_o\left(\gamma_e(Z_l\gamma_o - Z)e^{-\gamma_o l} - \gamma_o(Z_l\gamma_e - Z)e^{-\gamma_e l}\right)}{\gamma_e\left(\gamma_o^2 - \gamma_e^2\right)\left[\left(1 - \frac{Z_l}{Z_o}\right)e^{-\gamma_e l} + \left(1 + \frac{Z_l}{Z_o}\right)e^{\gamma_e l}\right]} \tag{16}$$

and

$$V_2 = \frac{k_o\left(\gamma_e(Z_l\gamma_o - Z)e^{-\gamma_o l} - \gamma_o(Z_l\gamma_e + Z)e^{\gamma_e l}\right)}{\gamma_e\left(\gamma_o^2 - \gamma_e^2\right)\left[\left(1 - \frac{Z_l}{Z_o}\right)e^{-\gamma_e l} + \left(1 + \frac{Z_l}{Z_o}\right)e^{\gamma_e l}\right]} \tag{17}$$

where $Z_o = \sqrt{Z/Y}$ is the characteristic impedance of the detector. The RF output power from the detector is the power developed in the output load Z_l

$$P_{\rm rf} = \frac{|V(l)|^2}{2Z_l}. \tag{18}$$

Fig. 4 shows a calculation of normalized electrical response as a function of frequency for several different optical absorption lengths using the open input boundary conditions of (15). In this calculation the detector is assumed to have $Z_o = Z_l = 50\ \Omega$, infinite length, perfect velocity match between the electrical signal and the light ($n_{\rm rf} = n_o = 3.5$), and no electrical propagation loss. All normalized responses in this paper are with respect to a conventional lumped photodetector of equivalent quantum efficiency, infinite bandwidth, and driving a 50 Ω load. Interestingly, there is a 6 dB drop in the TWPD's response with a characteristic frequency determined by the value of the optical absorption coefficient (α_o). The 6 dB asymptotic value at high frequencies indicates that the "effective" photocurrent is 1/2 of a lumped detector or, equivalently, the detector's responsivity (or quantum efficiency) is being halved. Since the detector's dc quantum efficiency is nearly 100%, the effective quantum efficiency at high frequencies is 50%.

The second set of boundary conditions, corresponding to terminating both ends of the detector, provides additional insight in detector operation. If both ends of the device are terminated in Z_o, the necessary boundary conditions are

$$\frac{V(l)}{I(l)} = -\frac{V(0)}{I(0)} = Z_o. \tag{19}$$

Applying this to (14) gives

$$V_1 = \frac{k_o(Z + \gamma_o Z_o)}{2(\gamma_e^2 - \gamma_o^2)} \tag{20}$$

and

$$V_2 = \frac{k_o(Z + \gamma_o Z_o)}{2(\gamma_e^2 - \gamma_o^2)} e^{-(\gamma_o + \gamma_e)\ell}. \tag{21}$$

Shown in Fig. 4 (labeled dual) is a calculation of normalized detector response as a function of frequency for several different optical absorption lengths using the boundary conditions set by (19). The same parameters are used as were used in the calculation for the single termination case. Here, a similar drop in response is seen except only a 3 dB reduction in signal occurs at high frequencies; however, this rolloff starts with a 3 dB lower low-frequency response as compared to the single termination case. The 3 dB reduction in response at low frequencies is consistent with applying two Z_o terminations in parallel to a lumped detector. Interestingly, these two reductions in combination result in a high-frequency response approaching the same value as the single termination case.

The dual termination response curves plotted in Fig. 4 include the power delivered to both terminations. It is informative to plot the response of the signal delivered to either termination separately. Fig. 5 shows the response of the signals from either port when $\alpha_o = 5$ cm^{-1}. Interestingly, the signal on the input termination (P_{RI}) rolls off at a rate of 20 dB/decade like a simple RC, whereas the signal on the output termination (P_{RO}) is frequency independent. The rolloff on the input side occurs at the transition frequency where the detector effectively becomes distributed. The -3 dB point exists where $\beta_o = \alpha_o$ or equivalently at

$$f_t = \frac{\alpha_o}{2\pi}\frac{c}{n_{\mathrm{rf}}} \tag{22}$$

where c is the speed of light and n_{rf} is the RF index of propagation along the detector. There is no signal at the input side of the detector at high frequencies. This explains why the single termination and dual termination solutions approach one another at high frequencies. One important result of the dual termination case is that a frequency independent response can be obtained by terminating both sides of the detector and only using the signal from the detector's output side.

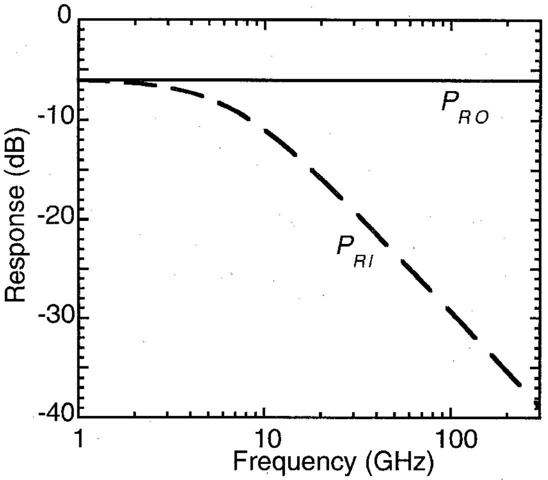

Fig. 5. Theoretical TWPD electrical response with $\alpha_o = 5$ cm^{-1} for both input load P_{RI} and output load P_{RO}.

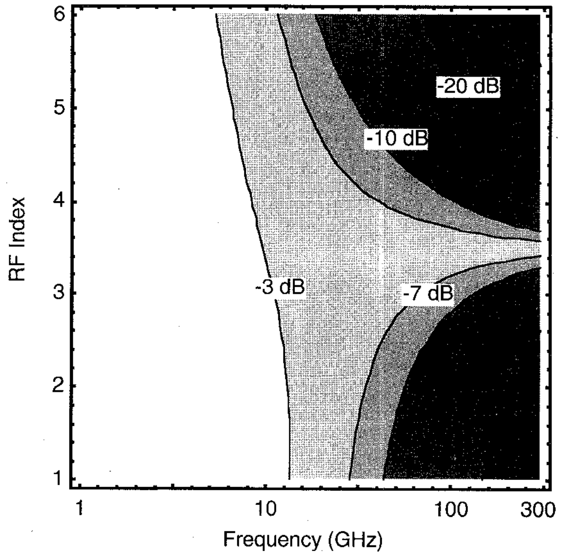

Fig. 6. Theoretical TWPD response as function of RF index and frequency. The same parameters were used as in Fig. 4 with $\alpha_0 = 5$ cm^{-1}.

To this point, all simulations have assumed a perfect velocity match. The model developed here is quite general and arbitrary velocity mismatches can be analyzed. Fig. 6 shows a contour plot of normalized response as a function of frequency and RF index. The optical index is fixed at 3.5 and the detector is terminated only on the output end. The RF index (c/v_p) is plotted from the speed of light ($n_{\mathrm{rf}} = 1$) to 1/6 the speed of light ($n_{\mathrm{rf}} = 6$). Slicing Fig. 6 along $n_{\mathrm{rf}} = 3.5$ produces the $\alpha_o = 5$ cm^{-1} single termination curve in Fig. 4. At low frequencies where the electrical wavelength exceeds $1/\alpha_o$, the RF index has little effect on the device's response since it is effectively electrically lumped. At very high frequencies, where the wavelength is much less than $1/\alpha_o$, the velocity match becomes critical as expected. Clearly, long high-frequency TWPD's need to be velocity matched to be effective.

IV. ELECTRODE DESIGN

As already stated, the detector's optical waveguide and electrodes must be designed for a velocity match. The propagation velocity of light in the waveguide is fixed by its dimensions and material composition. In a GaAs/AlGaAs material system

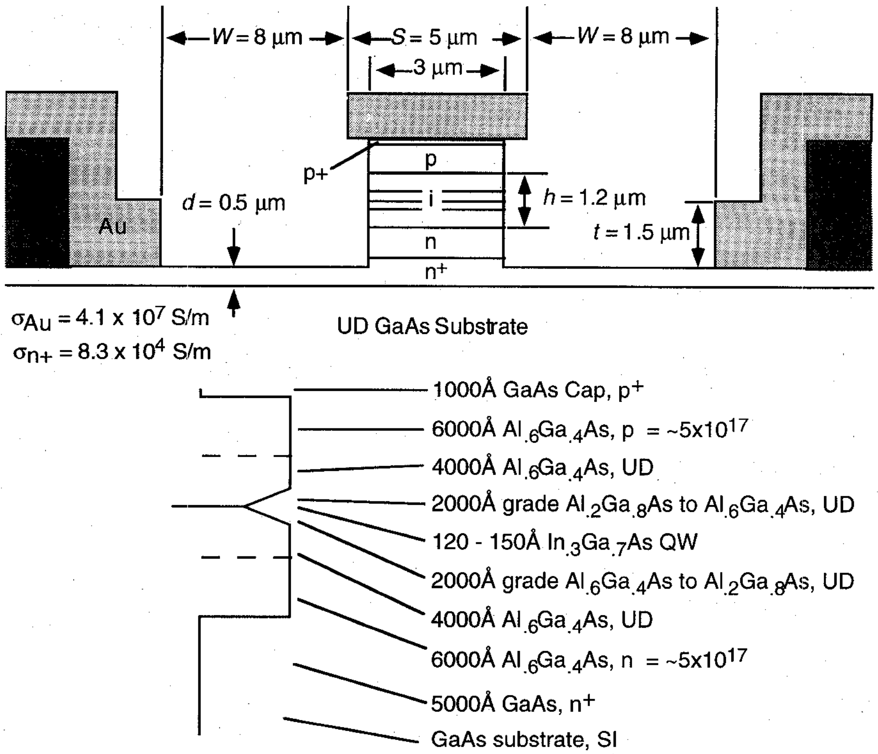

Fig. 7. Cross-section schematic of the TWPD for 1.06 μm operation (top) and diagram of material composition through the center axis of the waveguide (bottom). Dark areas are polyimide. UD means unintentionally doped.

the optical index will always be approximately 3.2. The actual optical velocity is not particularly critical since the RF-propagation velocity can be varied over a large range after the optical waveguide is designed. The metal electrode structure comprised of metal on top of the optical waveguide and ground planes to either side along with the "buried" heavily-doped n^+ layer, forms a slow-wave coplanar transmission line (see Fig. 7). The electrical propagation velocity of this transmission line is tunable over a large range by varying the line's dimensions. Hence, a velocity match can be achieved.

To achieve a velocity match and predict the detector's bandwidth, a model for electrical propagation along the detector is necessary. The type of transmission line formed in this detector is commonly called a "slow-wave coplanar waveguide" [12]. Such transmission lines require "full-wave" analysis for rigorous modeling [13]. For our purposes, quasi-TEM analysis [14] satisfactorily describes this line's properties.

The line's quasi-static impedance per unit length, Z, and admittance per unit length, Y, as shown in the equivalent circuit in Fig. 3 must be determined. Briefly, the inductance per unit length, L, is approximately that of a conventional coplanar waveguide. The capacitance, C, is estimated to be that of a parallel-plate capacitor. Assuming that the detector will be operated at large reverse bias, the semiconductor layers in the rib will be largely depleted. Then, semiconductor losses associated with transverse current flow can be included in the model as a series resistance, R_T, as shown in Fig. 3. The metal losses, Z_m, are assumed to be similar in form to those of a parallel plate waveguide and calculated as discussed in [14].

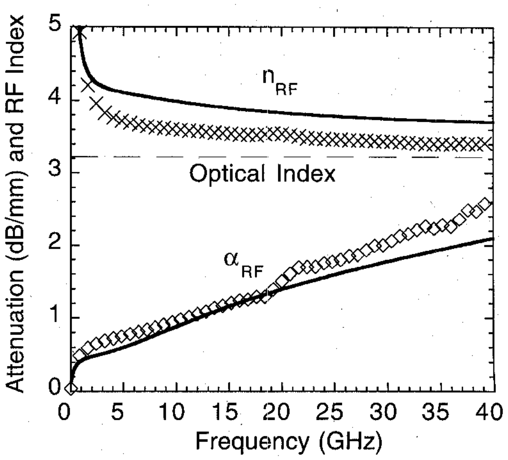

Fig. 8. Theoretical (symbols) and experimental (lines) microwave RF Index and attenuation at −20 V bias.

With the impedance, Z, and admittance, Y, known, the complex propagation constant, γ_e, and the complex characteristic impedance, Z_o, can be determined. A design was selected which offers a 50 Ω characteristic impedance and a velocity match to the light. The final structure is shown in Fig. 7. As seen in the next section, these dimensions are amenable to the optical design. Using these dimensions, the theoretical curves in Figs. 8 and 9 were generated.

Measurements of electrical propagation along the electrodes were performed by special test structures that have electrical probe contacts at both ends of the device. On-wafer microwave probes were then used to measure the electrode's two-port S-parameters. These S-parameters were then directly converted

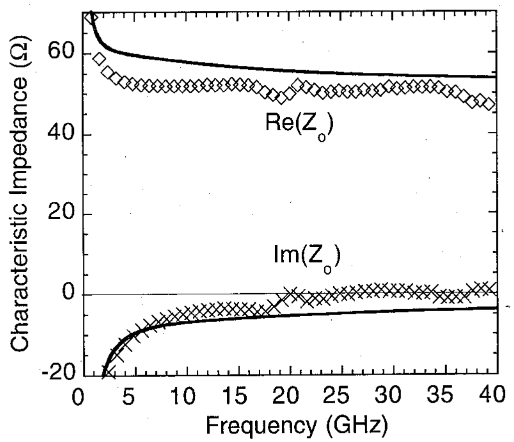

Fig. 9. Theoretical (symbols) and experimental (lines) microwave characteristic impedance at −20 V bias.

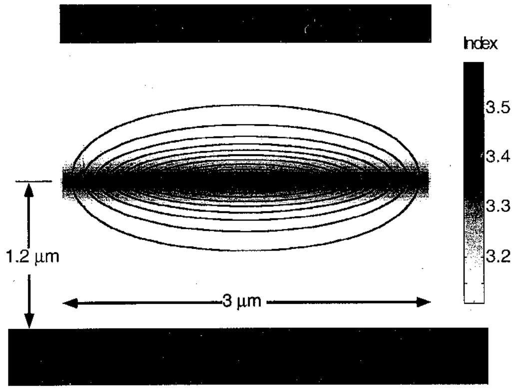

Fig. 10. Contour plot of constant electric field of the TE_{00} mode. Shading corresponds to Al mole fraction. Lighter gray is higher Al content. Contour values are 0.1 (outermost contour) to 0.9 (innermost contour) with a step of 0.1.

to transmission line parameters as described elsewhere [15]. Measurements on a 2.25-mm-long test device are summarized in Figs. 8 and 9.

In Fig. 8, an excellent correspondence is seen between the measured and experimental RF index with both being quite close to the desired optical index (3.2). Also in Fig. 8 are plots of the theoretical and experimental RF attenuation (dB/mm). Again an excellent correspondence exists. The attenuation is adequate for this application though device performance would improve if the attenuation could be further reduced. Since metal loss is dominant, the only practical method for reduction of the attenuation is to increase the center strip width. Fig. 9 shows a plot of the theoretical and experimental characteristic impedance which is quite close to 50 Ω. This 50 Ω impedance level allows this device to be easily inserted into conventional 50 Ω RF circuits/systems.

V. OPTICAL DESIGN

Our present design is optimized for 1.06 μm optical wavelength. The detector can be extended to other wavelengths by changing material systems. For example 1.55 μm operation could be obtained with an InGaAs quantum well on a InP substrate. All of the discussions here as well as the fundamental operation of this device are wavelength independent.

The key to proper optical design of a TWPD is to tailor the absorption length of the light in the waveguide so as to reduce the absorbed power density as discussed in this paper's first section. This is done by employing a single quantum well of GaAs or InGaAs with a high absorption coefficient within an otherwise transparent waveguide. Total waveguide loss is determined by the absorption coefficient of the quantum well multiplied by the percentage of total light in the waveguide that actually travels inside the quantum well (the overlap integral of the waveguide mode and the quantum well). The quantum well itself must be designed so that the electron-hole excitonic resonance occurs at the desired photon energy. This determines the width and composition of the quantum well. Our final quantum well design used 30% Indium and a 130 Å width to ensure that the absorption edge of the well is slightly lower in energy than the desired 1.064 μm operating wavelength. Room temperature absorption measurements show that the absorption coefficient of such strained quantum wells is ~1000 cm^{-1} at wavelengths slightly below the absorption edge wavelength.

As mentioned above, absorption of the waveguide mode is set by the overlap of the optical mode with the quantum well. We can adjust the overlap integral over a wide range through correct selection of the refractive index profile of the waveguide materials. We will not go into the details of the design approach other than to provide the complete detector design used in this work. Fig. 7 shows a cross-section schematic of our design for 1.06 μm wavelength while Fig. 10 shows the results of a two-dimensional simulation of the optical waveguide. The simulation includes effects of absorption in the quantum well and yields an optical modal index of 3.227 with a modal field absorption coefficient of 15 cm^{-1} assuming 1000 cm^{-1} absorption in the quantum well region. This absorption value leads to absorption of 98% of the initial light coupled into the waveguide within 1.25 mm of propagation length.

With the optical design selected, the RF propagation model and detector response model can be combined to predict real detector performance. The dimensions and parameters in Fig. 7 along with a device length of 1.25 mm, an optical absorption coefficient of 15 cm^{-1}, and an optical wavelength of 1.06 μm were used to generate the theoretical response plotted as the solid line in Fig. 11 (single output termination). The 6 dB rolloff as discussed previously is clearly present. An additional rolloff of a few dB due to RF propagation losses along the detector is also evident. The ripples at high frequencies are due to the finite length of the detector and slight impedance differences between the termination and the detector's characteristic impedance.

VI. DETECTOR FABRICATION

Microelectronic fabrication of the TWPD was as follows: the 3-μm-wide waveguide rib was defined by conventional contact-print photolithography using a positive-working tri-level etch mask [16]. The waveguides were etched using chlorine reactive-ion-beam etching [17] (RIBE) in a load-locked configuration for equal-rate etching of GaAs and AlGaAs

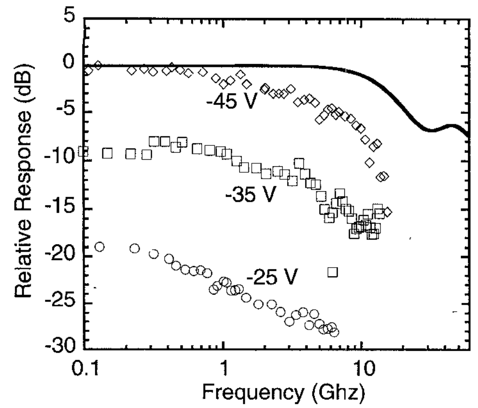

Fig. 11. Theoretical (line) and experimental (symbols) normalized electrical responses of the TWPD. Experimental curves are normalized to the low-frequency response at −45 V bias.

with smooth, vertical, sidewalls [18], and real-time etch depth monitoring [19] of the endpoint. The etch was extended to the interface between the lower AlGaAs cladding layer and the lower n^+-doped GaAs conductive layer. A second mask-etch step was then used to etch away the unneeded n^+ layer for device isolation. After etching, both p- and n-type ohmic contacts and the microwave transmission lines were formed using lift-off metallization.

VII. OPTICAL BANDWIDTH MEASUREMENTS

A two-laser optical heterodyne system was constructed for electrical bandwidth measurements. Nd:YAG lasers with <10 KHz linewidth at 1.06 μm were used for the light sources. A mode-hop-free RF-beat-frequency range of 60 GHz was obtained.

Fig. 11 shows a measured response from a 1.25 mm TWPD at several bias levels. This detector was operated with the input end electrically open and the output side terminated with the 50 Ω load (an RF spectrum analyzer). Bandwidth is seen to be approximately 4.8 GHz. This bandwidth is significantly less than that expected based on the theory derived in this paper ($\approx$14 GHz) and does not appear to be limited by the propagation losses along the electrodes, as indicated by the electrical propagation measurements. The present bandwidth limitation is believed to be in part due to dispersion in both the carrier generation and carrier transit time across the detector's depletion regions. The observed bias dependence is unusual for a conventional photodiode, but is expected here since the absorption occurs in a GaAs quantum well whose absorption edge is expected to red-shift as a function of applied bias due to the quantum-confined Stark effect. The bandwidth is largely bias independent indicating that avalanche multiplication does not influence device operation.

Including the 6 dB intrinsic response rolloff, the electrical losses along the detector, and the possible measurement errors, the response in Fig. 11 is not unreasonable. Longer devices were also measured and found to have similar bandwidths. Therefore, we believe present bandwidths to be limited by intrinsic photodiode properties. Future designs will have a thinner depletion width to reduce carrier transit times and dispersion for expected operation to much higher frequencies.

VIII. CONCLUSION

The TWPD, through its distributed nature, offers both high-frequency and high-power operation unavailable with conventional photodiode structures. The power capability of the TWPD should be only restricted by the catastrophic optical damage limit of the detector's facet. A detailed frequency-domain model for the electrical performance of the TWPD was developed. Measurements of electrical propagation along a TWPD were presented and found to compare well with theory. TWPD's were characterized using an optical heterodyning system. Though initial data on a large-sized $(3 \times 1250\ \text{m}^2)$ TWPD indicates low electrical bandwidth (4.8 GHz), future designs should allow for bandwidths in the millimeter-wave frequency regime.

ACKNOWLEDGMENT

The authors would like to thank B. Fuchs for her work in device fabrication and M. Housel for his extensive work in device characterization.

REFERENCES

[1] H. F. Taylor, O. Eknoyan, C. S. Park, K. N. Choi, and K. Chang, "Traveling wave photodetectors," *SPIE, Optoelectronic Signal Processing for Phased-Array Antennas II*, pp. 59–63, 1990.

[2] V. M. Hietala and G. A. Vawter, "Traveling-wave photodetector," U.S. Patent no. 5 270 532, Dec. 14, 1993.

[3] K. Giboney, R. Nagarajan, T. Reynolds, S. Allen, R. Mirin, M. Rodwell, and J. Bowers, "172 GHz, 42% quantum efficiency p-i-n travelling-wave photodetector," in *52nd Annual Device Research Conf.*, Boulder, CO, June 1994, postdeadline paper, pp. VIA-9.

[4] D. Jager and R. Kremer, "Travelling-wave optoelectronic devices for microwave applications," in *Proc. Int. 1994 IEEE MTT-S Topical Meet. Optical Microwave Interactions*, Nov. 21–23, 1994, pp. 11–14.

[5] G. A. Vawter and V. M. Hietala, "Unlimited-bandwidth distributed optical phase modulators and detectors: Design and fabrication issues," in *Proc. Int. 1994 IEEE MTT-S Topical Meet. Optical Microwave Interactions*, Nov. 21–23, 1994, pp. 3–6.

[6] M. Shur, *GaAs Devices and Circuits*. New York: Plenum, 1987, pp. 412–415.

[7] D. P. Bour, *Quantum Well Lasers*, P. S. Zory, Jr., Ed. Boston: Academic, 1993, p. 452.

[8] E. R. Brown, K. A. McIntosh, K. B. Nichols, M. J. Manfra, and C. L. Dennis, "Optical-heterodyne generation in low-temperature-grown GaAs up to 1.2 THz," *Proc. SPIE, Nonlinear Optics for High-Speed Electronics and Optical Frequency Conversion*, vol. 2145, pp. 200–208, Jan. 26–27, 1994.

[9] V. M. Hietala, G. A. Vawter, T. M. Brennan, B. E. Hammons, and W. J. Meyer, "Optical generation of radio-frequency power," Sandia Report SAND94-2761, National Technical Information Service, Springfield, VA, Nov. 1994.

[10] V. M. Hietala and G. A. Vawter, "A large-bandwidth high-quantum-efficiency traveling-wave photodetector base on a slow-wave coplanar transmission line," presented at *Progress in Electromagnetic Research Symp.*, Boston, MA, July 1–5, 1991.

[11] K. S. Giboney, M. J. W. Rodwell, and J. E. Bowers, "Traveling-wave photodetectors," *IEEE Photon. Technol. Lett.*, vol. 4, pp. 1363–1365, Dec. 1992.

[12] H Hasegawa and H. Okizaki, "M.I.S. and schottky slow-wave coplanar striplines on GaAs substrates," *Electron. Lett.*, vol. 13, no. 22, pp. 663–664, Oct. 1977.

[13] Y. Fukuoka, Y. Shin, and T. Itoh, "Analysis of slow-wave coplanar waveguide for monolithic integrated circuits," *IEEE Trans. Microwave Theory Tech.*, vol. 31, pp. 567–573, 1983.

[14] Y. R. Kwon, V. M. Hietala, and K. S. Champlin, "Quasi-TEM analysis of slow-wave mode propagation on coplanar microstructure MIS

transmission lines," *IEEE Tans. Microwave Theory Tech.*, vol. 35, pp. 545–551, 1987.

[15] V. M. Hietala and K. S. Champlin, "Measurement of the microwave properties of micron-sized coplanar transmission lines," *J. Electromagnetic Waves and Applications*, vol. 5, no. 4/5, pp. 439–452, 1991.

[16] G. A. Vawter, L. A. Coldren, J. L. Merz, and E. L. Hu, "Nonselective etching of GaAs/AlGaAs double heterostructure laser facets by Cl_2 reactive ion etching in a load-locked system," *Appl. Phys. Lett.*, vol. 51, no. 10, pp. 719–721, 1987.

[17] K. Asakawa and S. Sugata, "GaAs and GaAlAs equi-rate etching using a new reactive ion beam etching system," *J. Japan Appl. Phys.*, vol. 22, no. 10, p. L653, 1983.

[18] G. A. Vawter, J. F. Klem, G. R. Hadley, and S. H. Kravitz, "Highly accurate etching of ridge-waveguide directional couplers using in-situ reflectance monitoring and periodic multilayers," *Appl. Phys. Lett.*, vol. 62, no. 1, pp. 1–3, 1993.

[19] G. A. Vawter, J. F. Klem, and R. A. Leibenguth, "Improved epitaxial layer design for real-time monitoring of dry-etching in III—V compound heterostructures with depth accuracy of ±8 nm," *J. Vac. Sci. Technol.*, vol. A 12, no. 4, 1994.

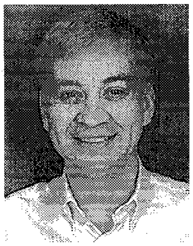

Vincent M. Hietala (S'85–M'88) received the B.S.E.E. degree with High Distinction, M.S.E.E., and Ph.D. degrees in electrical engineering from the University of Minnesota in 1983, 1987, and 1988, respectively.

In 1988, he was with Honeywell's Sensors and Signal Processing Laboratory, Bloomington, MN. There, he worked as a Research Scientist on modeling optical waveguides and on the development of high speed optical data links. Since 1988, he has been a Senior Member of Technical Staff in the compound-semiconductor technology department at Sandia National Laboratories, Albuquerque, NM. His current research activities include the development of high-speed electronic and optoelectronic devices and microwave/millimeter wave measurement techniques.

G. Allen Vawter (S'86–M'87) received the B.S., M.S., and Ph.D. degrees in electrical engineering from University of California, Santa Barbara, in 1982, 1983, and 1987, respectively.

During his graduate work at the University of California he studied reactive-ion-etching of GaAs/AlGaAs laser diode facets and integration of laser diodes into waveguide circuits. He then joined Sandia National Laboratories in Albuquerque, NM, and is currently a Senior Member of Technical Staff. His research interests include design and fabrication of diode lasers and optoelectronic integrated circuits in III–V compound semiconductors as well as application of reactive-ion-beam etching in the fabrication of novel opto-electronic devies.

Dr. Vawter is a member of Tau Beta Pi, Eta Kappa Nu, and the American Vacuum Society.

T. M. Brennan, photograph and biography not available at the time of publication.

B. E. Hammons, photograph and biography not available at the time of publication.